

## **Short term collaborations of the NEAMS Center of Excellence: third wave**

---

**Nuclear Science and Engineering Division**

### **About Argonne National Laboratory**

Argonne is a U.S. Department of Energy laboratory managed by UChicago Argonne, LLC under contract DE-AC02-06CH11357. The Laboratory's main facility is outside Chicago, at 9700 South Cass Avenue, Argonne, Illinois 60439. For information about Argonne and its pioneering science and technology programs, see [www.anl.gov](http://www.anl.gov).

### **DOCUMENT AVAILABILITY**

**Online Access:** U.S. Department of Energy (DOE) reports produced after 1991 and a growing number of pre-1991 documents are available free at OSTI.GOV (<http://www.osti.gov/>), a service of the US Dept. of Energy's Office of Scientific and Technical Information.

### **Reports not in digital format may be purchased by the public from the National Technical Information Service (NTIS):**

U.S. Department of Commerce  
National Technical Information Service  
5301 Shawnee Rd  
Alexandria, VA 22312  
**[www.ntis.gov](http://www.ntis.gov)**  
Phone: (800) 553-NTIS (6847) or (703) 605-6000  
Fax: (703) 605-6900  
Email: **[orders@ntis.gov](mailto:orders@ntis.gov)**

### **Reports not in digital format are available to DOE and DOE contractors from the Office of Scientific and Technical Information (OSTI):**

U.S. Department of Energy  
Office of Scientific and Technical Information  
P.O. Box 62  
Oak Ridge, TN 37831-0062  
**[www.osti.gov](http://www.osti.gov)**  
Phone: (865) 576-8401  
Fax: (865) 576-5728  
Email: **[reports@osti.gov](mailto:reports@osti.gov)**

### **Disclaimer**

This report was prepared as an account of work sponsored by an agency of the United States Government. Neither the United States Government nor any agency thereof, nor UChicago Argonne, LLC, nor any of their employees or officers, makes any warranty, express or implied, or assumes any legal liability or responsibility for the accuracy, completeness, or usefulness of any information, apparatus, product, or process disclosed, or represents that its use would not infringe privately owned rights. Reference herein to any specific commercial product, process, or service by trade name, trademark, manufacturer, or otherwise, does not necessarily constitute or imply its endorsement, recommendation, or favoring by the United States Government or any agency thereof. The views and opinions of document authors expressed herein do not necessarily state or reflect those of the United States Government or any agency thereof, Argonne National Laboratory, or UChicago Argonne, LLC.

**Short term collaborations of the NEAMS Center of Excellence: third wave**

---

prepared by

Ling Zou, Jun Fang, Rui Hu, Daniel O'Grady, and Dillon Shaver

Nuclear Science and Engineering Division, Argonne National Laboratory

August 31, 2021

## Executive Summary

The mission of the NEAMS Center of Excellence for Thermal-fluids Applications in Nuclear Energy is to advance the goals of the NEAMS program by providing leadership, best practices, research, and support and training for computational thermal hydraulics. In particular NEAMS tools are being developed to ultimately span the entire range of length- and time-scales required for a comprehensive reactor design and safety analysis. The focus of The Center is on the use, best practices, and deployment to stakeholders of the thermal hydraulic codes.

The Center of Excellence, originally launched in 2018, has as its key goal to serve as a “front door” to industry. As part of this goal, The Center is in its third year of a program to start collaborative efforts between the laboratories and industry with the objective of stimulating cooperation and increasing the adoption of thermal hydraulics tools developed under NEAMS by the industry at large. With an overwhelmingly positive response from participants, previous short-term projects have lead to more in-depth collaborations.

This year, two industry partners participated in the third wave of collaborations aimed at demonstrating the value of the NEAMS T/H tools. These are Oklo and Westinghouse. Oklo proposed a demonstration of a thermal energy storage system applied to an SFR and Westinghouse proposed a demonstration of direct resolution of wall surface roughness, aimed at improving the manufacture of accident tolerant fuels for LWRs. In this report we present the results of these collaborations.



# Contents

Executive Summary . . . . .	i
List of Figures . . . . .	iv
List of Tables . . . . .	v
1 Introduction . . . . .	1
2 Oklo Project: An Integrated SFR/TES System for Load Following . . . . .	2
2.1 Introduction . . . . .	2
2.2 Integrated SFR/TES System . . . . .	3
2.3 Reference Market and Load Following Scenario . . . . .	5
2.4 TES Tank Sizing and Design . . . . .	7
2.5 SAM Input Model . . . . .	10
2.6 Simulation Results on a ‘Typical Day’ . . . . .	15
2.7 Conclusions and Future Work . . . . .	15
3 Westinghouse Project: Direct resolution of surface roughness . . . . .	16
3.1 Introduction . . . . .	16
3.2 Flow solver: Nek5000 . . . . .	17
3.3 Problem Description . . . . .	18
3.4 Results . . . . .	20
3.5 Conclusions . . . . .	24
Acknowledgments . . . . .	25
References . . . . .	29

# List of Figures

1.1	Potential paths for industry collaboration with The Center . . . . .	1
2.1	Schematic view of ABTR primary system . . . . .	3
2.2	(a) The layout of heat transport for the original ABTR design with the Rankine cycle for power conversion; (b) The layout of heat transport for the proposed integrated SFR/TES system. . . . .	5
2.3	PJM generation fuel mix data in April of 2021. . . . .	6
2.4	PJM gas generation data in April of 2021. . . . .	7
2.5	With simplified assumption, the load following for an individual SFR/TES system. . . . .	8
2.6	The layout of the integrated SFR/TES system. . . . .	10
2.7	Schematic drawing of SFR/TES SAM input model. . . . .	11
2.8	TES tank model using SAM. . . . .	12
2.9	Westinghouse four-loop design response during a 100%-50% ramp load decrease transient . . . . .	13
2.10	Typical 1200 MWe Pressurized Water Reactor Plant Cycle Efficiency vs. Power Level . . . . .	14
2.11	Hot leg pump heat control strategy based on monitored steam generator heat rejection rate and electricity demand. . . . .	14
2.12	SAM simulation results on a ‘typical day,’ using proposed April 5 load following data shown in Figure 2.5. . . . .	15
3.1	Cross-sectional view of the computational mesh at a polynomial order, $N = 7$ : (a) overview, (b) zoom-in view. . . . .	19
3.2	The rough pipe mesh with staggered roughness elements on the wall surface. . . . .	20
3.3	Cross-sectional view of the computational mesh from the mesh morphing. . . . .	21
3.4	Detailed view on the mesh around the wall roughness elements. . . . .	22
3.5	A snapshot of the instantaneous velocity field from the smooth pipe DNS. . . . .	23
3.6	Mean axial velocity in the near wall region from the smooth pipe DNS. . . . .	23
3.7	Comparison of the velocity field from the smooth and rough pipes in the axial direction. . . . .	24
3.8	Circulations observed around the wall roughness elements. . . . .	24

3.9	A rough pipe modeling surface roughness elements as cavities. . . . .	25
-----	---	----

# List of Tables

2.1	ABTR design parameters . . . . .	4
2.2	TES tank design parameters . . . . .	9
2.3	TES tank wall material properties . . . . .	12
3.1	Darcy friction factors in pipe geometry ( $Re = 5,300$ , $\epsilon = 0.04$ ) . . . . .	25

# 1 Introduction

A primary goal of the Department of Energy’s Nuclear Energy Advanced Modeling and Simulation (NEAMS) program is to develop the next generation of simulations tools to support the design and deployment of commercial nuclear power. The mission of the NEAMS Center of Excellence for Thermal-fluids Applications in Nuclear Energy is to advance this goal by providing leadership, best practices, research, and support and training for computational thermal-fluids applications in nuclear energy. This is accomplished by leveraging expertise in the NEAMS tools to solve challenging problems in fluid flow and heat transfer. The NEAMS tools provide simulation capabilities covering a range of temporal and spatial scales and the Center connects stakeholders in industry with the expertise to use these tools to their fullest. This addresses a pressing need, facilitating advanced reactor development and commercialization.

Building on the success of previous years [1, 2], The Center continues to serve as an avenue of engagement for industry with a low barrier to entry, serving as a true “front door”. The Center strives to make the full suite of NEAMS TH tools available to industry stakeholders. This is accomplished through center meetings, training, and more directly through short-term collaboration projects. We note that these short term projects are not aimed at providing a funding venue and cannot be used to address problems requiring the use of protected IP. These collaborations are intended to serve as a launching point for a more in-depth collaboration, leading to a partnership for a larger proposal, such as through GAIN or other funding opportunity announcements (FOAs), which can involve the use of protected IP. The potential paths of industrial customers are outlined in the diagram below, reflecting the different levels of commitment from the industry partner.

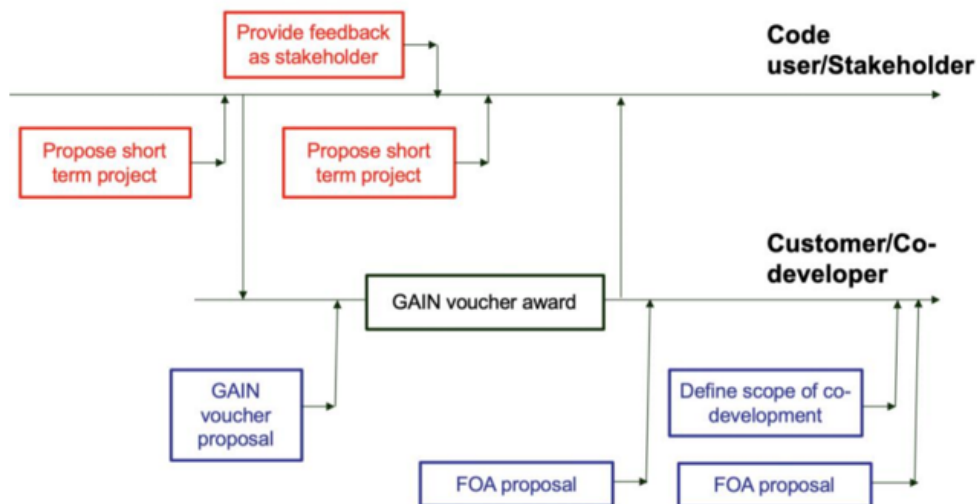


Figure 1.1: Potential paths for industry collaboration with The Center

This year The Center completed its third wave of collaboration projects with Oklo and Westinghouse. Oklo proposed a demonstration of an integrated load following system based on thermal energy storage for a sodium fast reactor. The Westinghouse project focused on the direct resolution

of wall surface roughness aimed at improving the manufacture of accident tolerant fuels. Results of these collaborations are detailed in the following sections.

## 2 Oklo Project: An Integrated SFR/TES System for Load Following

### 2.1 Introduction

Traditionally, nuclear power plants have been designed and used extensively as base load sources of electricity. This has been generally recognized as the most economical, because of their high capital but low operational cost, and technically simple mode of operation [3, 4]. For countries/states with large shares of nuclear energy or electricity markets with high renewable energy penetration, it is desirable to have nuclear power plants capable of load following. As an example, in France where about 70% of its electricity derived from nuclear energy [5], load following is practiced in commercial PWR operations on a regular basis, including daily variations of the power demand [3]. Such load following maneuvering is typically achieved by varying reactor power output. For example, “grey” rods are used in PWRs for reactor power control during load following [3, 6]. This kind of load following operation mode decreases nuclear power plants’ annual energy output. The resulting reduced capacity factor of a cycling plant increases the difficulty of capital recovery [7] because nuclear power plants, unlike their fossil power plants counterparts, do not benefit from saving fuel cost by reducing power output.

An alternative pathway for nuclear power plants load following is to focus on the thermal energy storage (TES) system, as suggested by several research, e.g., [7, 8, 9, 10, 11] among many others. An additional thermal energy storage system to the nuclear reactor is able to store the excessive thermal energy when electricity demand is low; and provides peaking output when the demand is high. The integration of nuclear reactors with thermal energy storage system would allow nuclear power plants to provide load following capability while still operating at a relatively constant power output. This load following strategy reduces the economic penalty associated with reducing reactor power output used in the previously discussed load following strategy. In addition, a significant amount of experience and knowledge on thermal energy storage systems has been acquired in the solar power industry, where large scale commercial TES systems have been deployed and operated [12]. A recent major development is TerraPower’s Sodium technology, which “features a 345MWe reactor combined with a gigawatt-scale thermal energy storage system that can be optimized for specific markets” [13]. Other advanced reactor designers, including Oklo, are also interested in a similar concept of an integrated nuclear reactor and TES system for load following capability.

Under the support of DOE-NE’s Nuclear Energy Advanced Modeling and Simulation (NEAMS) - Center of Excellence for Thermal Fluids Applications in Nuclear Energy, an effort had been pursued to support Oklo’s needs in the modeling and simulation of an integrated sodium fast reactor (SFR) and TES system using SAM [14] as the system analysis tool. The main focuses of this study are to establish modeling capability for the proposed integrated SFR/TES system, and to model the integrated system’s behavior in response to time-varying grid demand, and based on time-varying grid demand data, to estimate sizing for energy storage components and pump flow rates. Another important task is to identify gaps in modeling and simulation capabilities for future work.

## 2.2 Integrated SFR/TES System

In this study, an integrated SFR/TES system has been proposed to include the Advanced Burner Test Reactor (ABTR) [15] as the reference SFR and storage tanks in ABTR's intermediate heat transport loop for thermal storage.

The ABTR is a 250 MWt liquid sodium-cooled pool-type fast reactor designed by Argonne National Laboratory as an integral part of the Global Nuclear Energy Partnership (GNEP). The technical details of the ABTR is documented in the preconceptual design report [15]. The primary system of the ABTR is configured in a pool-type arrangement, with the reactor core, primary pumps, intermediate heat exchangers (IHX), and direct reactor auxiliary cooling system (DRACS) heat exchangers all immersed in a pool of sodium coolant within the reactor vessel, as illustrated in Figure 2.1.

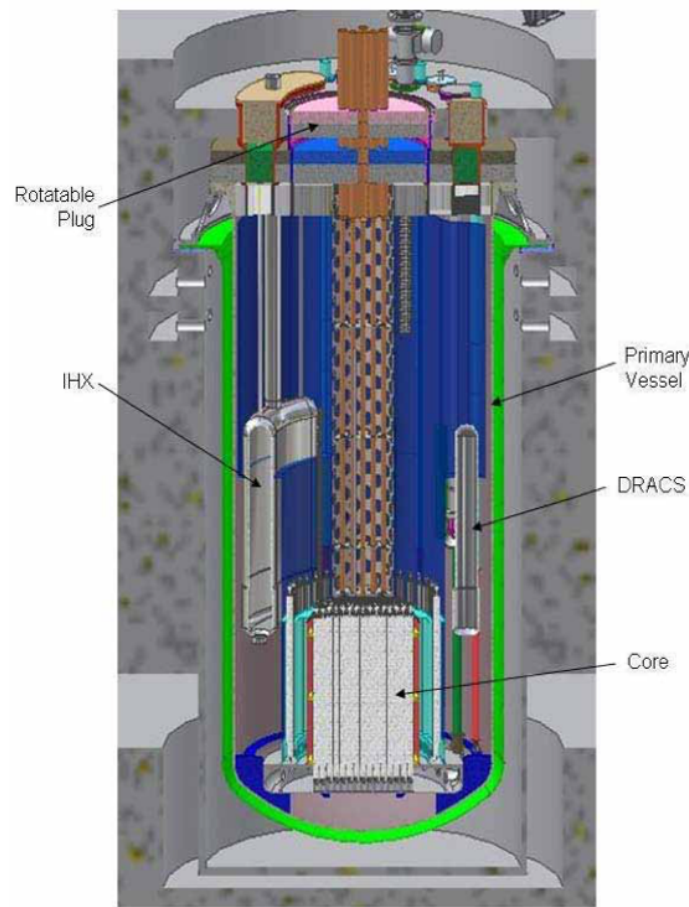


Figure 2.1: Schematic view of ABTR primary system [15].

Within the reactor vessel, primary electromagnetic pumps are used to drive sodium flow from the cold pool into the inlet plenum at the bottom of the core. The cold sodium is heated as it flows through the core and exits the core into the outlet plenum at the top of the core. The hot sodium

Table 2.1: ABTR design parameters

Primary System	
Reactor Power	250 MWt
Coolant	Sodium
Mass Flow Rate	628 kg/s
Coolant Inlet/Outlet Temperatures	355/510 °C
Intermediate Loop	
Number of IHX	2
IHX Capacity	125 MWt
Primary Sodium Inlet/Outlet Temperatures	510/355 °C
Primary Sodium Mass Flow Rate	628 kg/s
Secondary Sodium Inlet/Outlet Temperatures	333/488 °C
Secondary Sodium Mass Flow Rate	628 kg/s
Power Conversion System	
Type	Steam Rankine Cycle
Number of Steam Generators	2
Steam Generators Capacity	125 MWt
Steam Exit Pressure	155 bar
Water/Steam Inlet/Outlet Temperatures	216/454 °C
Cycle Efficiency	37.8 %

risers in the hot pool and enters the inlet of the intermediate heat exchangers, where the hot sodium rejects the heat to the intermediate loop, and then returns to the cold pool. This forms the closed flow ‘loop’ for the primary sodium in the reactor vessel.

The current ABTR design adopts two possible options for its power conversion system, i.e., an innovative supercritical CO<sub>2</sub> (sCO<sub>2</sub>) Brayton cycle as the reference design, and a superheated steam Rankine cycle as the alternative design. In the intermediate sodium loop, the sodium absorbs heat from the primary side hot sodium in the IHXs, and then releases the heat to working fluid of the power conversion system through a sodium-to-CO<sub>2</sub> (Na-to-CO<sub>2</sub>) heat exchanger in the Brayton cycle design, or a steam generator (SG) in the Rankine cycle design. In this study, the Rankine cycle has been adopted for the proposed integrated SFR/TES system as suggested by Oklo. Compared with the sCO<sub>2</sub> Brayton cycle, the steam Rankine cycle is a well developed technology, and abundant experience has been acquired on its load following performance from commercial PWR operations. Figure 2.2a shows the schematic layout of the heat transport of the ABTR with the Rankine cycle design. Several important ABTR design parameters are summarized in Table 2.1.

For the thermal energy storage, as discussed in [9], multiple viable solutions for sodium-cooled reactors are possible. First, sodium itself can be used as heat storage medium because of its high boiling point and excellent heat transfer characteristics. The simplest design would be a



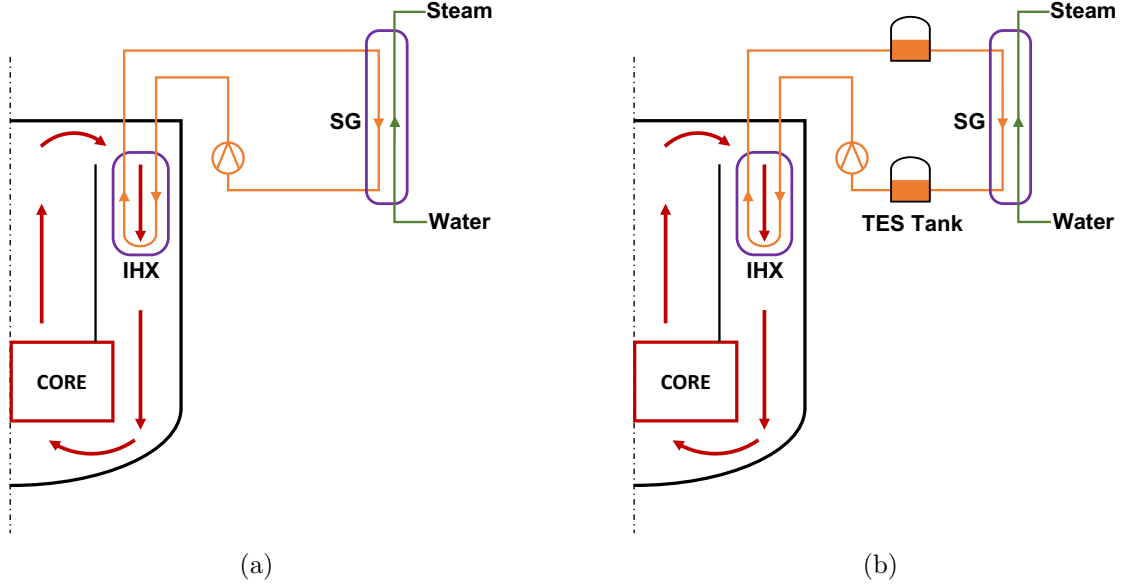


Figure 2.2: (a) The layout of heat transport for the original ABTR design with the Rankine cycle for power conversion; (b) The layout of heat transport for the proposed integrated SFR/TES system.

two-tank direct system, in which the sodium is stored in two tanks - one at high temperature and the other at low temperature. In the 1980s, sodium has already been tested as heat transfer and storage fluid in a central receiver system in the IEA-SSPS (International Energy Agency's Small-Solar-Power-System-Project) in Almeria, Spain, although with a relatively small heat storage capacity of 5 MWh [16]. Other options, such as single tank heat storage, are also possible, as discussed in [9]. Sodium-compatible materials, such as iron and steel, can also be used as heat storage medium. This approach reduces the total inventory of sodium, which improves the safety of the storage system, since sodium is highly reactive with air, water, and many other materials [9]. For this study, Oklo suggested both options, i.e., sodium or stainless steel, as the heat storage medium. Due to the limited work scope of this study, we have pursued the heat storage option that uses sodium in the two-tank direct system. As a result, the integrated SFR/TES system proposed in this study includes the ABTR as the reference reactor design, a two-tank direct system as the thermal energy storage, and the steam Rankine cycle as the power conversion system. The proposed SFR/TES system is illustrated in Figure 2.2b. Under this design, load following is realized by adjusting the mass flow rate from the hot leg tank to the steam generator, while reactor can still maintain a relatively constant operating condition. When the demand is lower than reactor nominal power output, thermal energy is stored in the hot leg tank, and when the demand is higher, stored thermal energy is used to produce higher-than-nominal output.

## 2.3 Reference Market and Load Following Scenario

It is important to discuss the integrated SFR/TES system as a load following power plant in a target market. In this study, we have chosen PJM Interconnection as the reference electricity market, which

includes the great Chicago area where Argonne National Laboratory is located. PJM is a regional transmission organization (RTO) that coordinates the movement of wholesale electricity in parts of the northeast and midwest U.S., serving more than 65 million people [17]. PJM’s energy market operates like a stock exchange, by matching supply and demand, electricity price is established [18]. For this study, we are particularly interested in the time varying electricity data, for example, total grid load, generation fuel mix, etc. These data provide a reference electricity market to study the deployment of the proposed integrated SFR/TES system, and load following scenario where the proposed integrated system can be tested.

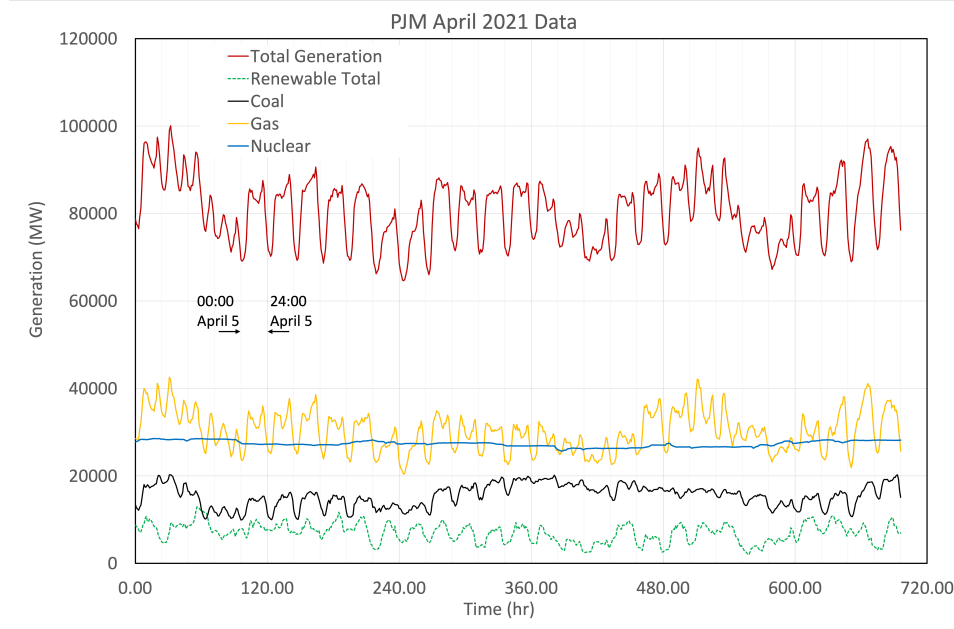


Figure 2.3: PJM generation fuel mix data in April of 2021.

Figure 2.3 shows the PJM generation fuel mix data in April of 2021. The source data used to generate the plot are provided online by PJM, which can be accessed at <http://dataminer2.pjm.com>. The total electricity generation is from many different types of fuel sources, including nuclear, gas, coal, renewable, etc. Figure 2.3 plots the total generation along with several major contributors. Several observations can be made from this plot. The total electricity generation, also total load, shows daily oscillation, reflecting the demand change between daytime (high demand) and nighttime (low demand). Note that April 5 of 2021 was a Monday. From the plot, it can also be seen that the demand during weekdays is higher than during weekends. The daily oscillation of total electricity demand exhibits around 10% of oscillation, which is, in absolute value, still significant enough and necessitates the deployment of load following electricity source. As shown in Figure 2.3, gas plants are such load following plants that follow closely the daily oscillatory electricity demand. On the other hand, electricity from existing nuclear power plants is stable, which is not surprising as they operate as base load source. Total electricity from renewable sources, ‘Renewable Total’ as shown in Figure 2.3, including solar, wind, hydro, and ‘other renewables,’ contributes a relatively small fraction to the total generation, meaning that PJM is not a market with high renewable penetration.

If we intend to deploy the proposed integrated SFR/TES system into the PJM electricity market,

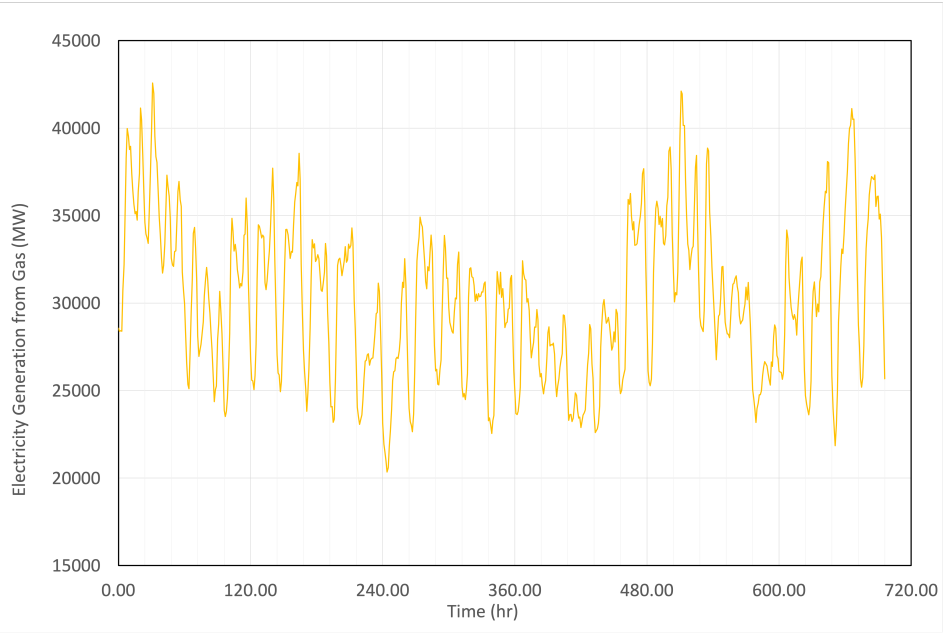


Figure 2.4: PJM gas generation data in April of 2021.

the system must be able to compete with the already existing load following plants, i.e., those gas plants. This means that the proposed integrated system will be able to follow the load as the existing gas plants can do, as shown in Figure 2.4 for the April gas plants data. Because of the large amount of electricity generated by the gas plants, it will clearly take a fleet of the proposed system to feel the gap. Instead, if it is argued that such an integrated system could be deployed one by one, and a simple assumption could be made that each of this newly deployed system will follow the electricity demand *proportional* to what is shown in Figure 2.4. This leads to Figure 2.5, which shows proposed load following behavior of an individual SFR/TES system. On average, the individual SFR/TES system delivers a nominal power at 250MWt, while it ramps up or down by pumping or storing sodium in the two TES tanks.

## 2.4 TES Tank Sizing and Design

The size of TES tanks is determined by many factors, including the desired total storage heat capacity, heat storage medium thermal properties, temperature difference between the hot and cold tanks, mechanical strength of tank materials, economics, etc. Ignoring the mechanical and economical limits, the size (volume in [m<sup>3</sup>]) of TES tanks can be simply computed as

$$V = \frac{Q}{\rho c_p (T_{hot} - T_{cold})}, \quad (1)$$

in which,  $Q$  the total storage capacity in [J], while MWh and GWh are more commonly used in engineering designs,  $\rho$  the storage medium density in [kg/m<sup>3</sup>],  $c_p$  the storage medium specific

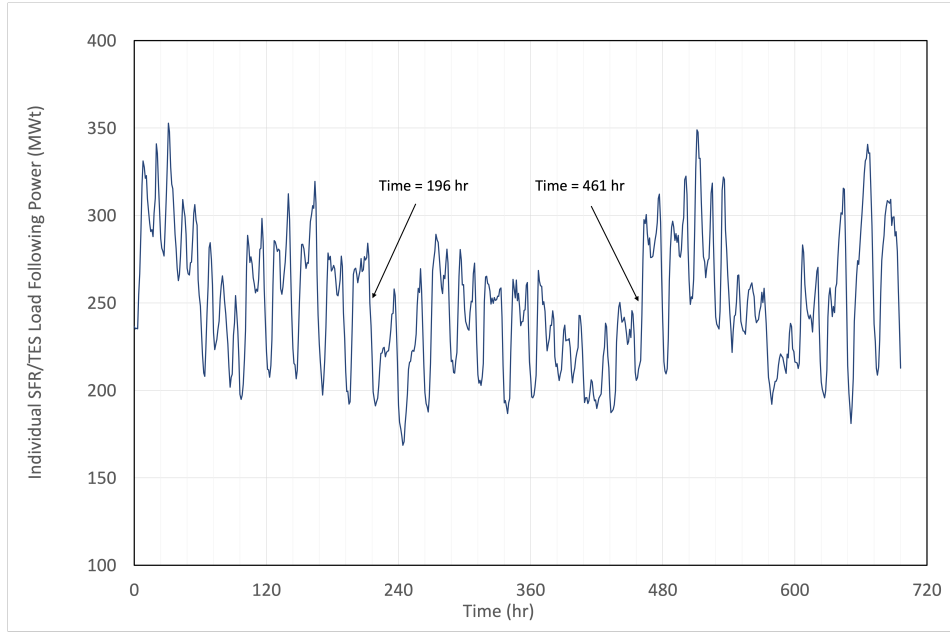


Figure 2.5: With simplified assumption, the load following for an individual SFR/TES system.

heat capacity in [J/kg-K],  $T_{hot}$  and  $T_{cold}$  the storage medium temperatures in hot and cold tanks, in [K]. For this proposed system, using sodium as the thermal storage medium, the following numbers can be used to estimate the tank sizing,  $\rho \sim 1000$  kg/m<sup>3</sup>,  $c_p \sim 1230$  [J/kg-K],  $T_{hot} = 488$  °C, and  $T_{cold} = 333$  °C. With all these numbers are fixed, the tank size solely depends on the required total storage capacity, which in turn determined by how load following will be performed. As an extreme example, let's assume that during the entire April, the nuclear reactor will operate in a constant condition, while the integrated system will be able to follow the load as shown in Figure 2.5. For an arbitrary time period ( $\Delta t$ ) starting from an arbitrary time point ( $t$ ), the required storage capacity is to find the difference between the integrated power generation and nominal power generation, i.e.,

$$q(t; \Delta t) = \left| \int_t^{t+\Delta t} (P(t) - \bar{P}) d\tau \right|, \quad (2)$$

in which,  $P(t)$  is the output power of the integrated system, and  $\bar{P}$  is the nominal output power, which is 250 MWt in our case. The required total storage capacity for this extreme example is then to find the maximum value of all possible  $q(t; \Delta t)$  values, i.e.,

$$Q = \max\{q(t, \Delta t)\} \quad \text{for any } t \text{ and } \Delta t. \quad (3)$$

Apply the above equation to the April load following data shown in Figure 2.5, we can estimate the required total storage capacity to be about 6.5 GWh (between 196 to 461 hr). Using Equation 2, the estimated tank size is about  $1.2 \times 10^5$  m<sup>3</sup>. This is clearly not a practical solution, and the extreme condition constraint should be removed. A more practical load following strategy is to

Table 2.2: TES tank design parameters

Tank Shape	Cylinder
Diameter	36 m
Height	14 m
Wall Material	Steel
Wall Thickness	4 cm
Insulation Material	Mineral Wool
Insulation Thickness	40 cm

allow for nuclear reactor power output to vary, but with much reduced frequency, such as once per day or week, to minimize the economic penalty associated with reduced reactor power reduction. With this strategy, the TES capacity needs only cover the fluctuation of electricity demand for one day, and reactor power needs to adjust once per day, or less, if the daily electricity demand pattern does not change significantly. For example, if we take April 5th as a ‘typical day,’ the estimated thermal storage capacity need is only about 376 MWh, almost 20 times less than the 6.5 GWh needed for the extreme assumption.

The nuclear community has a long history of successful handling liquid sodium. Sodium is relatively noncorrosive and compatible with normal materials of construction such as austenitic and ferritic steels [19]. As an example, the ABTR reactor vessel is constructed of austenitic stainless steel [15]. For large volume storage, there are additional considerations related to isolation, moisture protection, fire protection, etc. [19], which will not be further explored in this study. As for tank design, many experience can be leveraged from the solar power industry, where large size solar salt thermal storage tanks, with storage capacity in the magnitude of GWh, are constructed and operated. In this study, based on preliminary calculation, a reference heat storage tank design is adopted from Andasol parabolic trough power plants based on open literature information [20, 21, 22]. The Andasol project thermal storage tank is a cylinder shape tank, with a diameter of 36 m, and a height of 14 [m], and uses solar salt as the heat storage medium. The total storage capacity is around 1 GWh [12]. The same tank will provide approximately 653 MWh heat storage capacity for our proposed SFR/TES system because of different heat storage medium and operating temperatures. The reference tank design parameters are summarized in Table 2.2, which are largely based on the design information provided in [21].

Because of the size of the tank and the large volume sodium stored in them, it is proposed to install both tanks on the ground level in a distance from the below grade nuclear reactor. As a primary design, the piping system connecting the IHX, storage tanks, and steam generator is comprised of 14-inch schedule 40s stainless steel pipes insulated with the same mineral wool material. In a realistic dimension, the layout of the proposed SFR/TES system is illustrated in Figure 2.6.

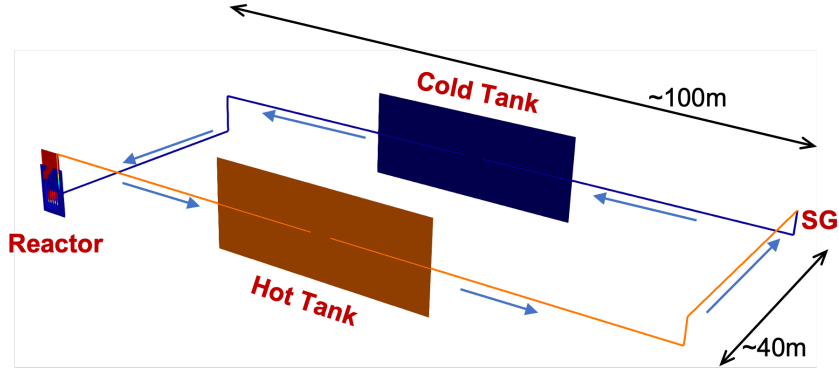


Figure 2.6: The layout of the integrated SFR/TES system.

## 2.5 SAM Input Model

The SAM input model for the proposed SFR/TES system includes three essential subsystems, i.e., the ABTR core, TES tanks, and the simplified steam generator. Control systems that control the intermediate loop pumps are also essential to model the load following performance of the integrated system. The input model is schematically illustrated in Figure 2.7.

The ABTR input model is developed based on a previous work that studied the transient behavior of ABTR [23]. Some changes and simplifications are made, e.g., the direct reactor auxiliary cooling system (DRACS) is not included in this current model, as it is not relevant to the load following study. The original input model of the ABTR is detailed in [23] and will only be briefly discussed here. Based on reactor physics calculation, a five-channel model was selected to model the reactor core. Each of the five core channels represents a group of fuel assemblies with different characteristics. For example, channel 1 represents the peak-power inner-core subassembly with fresh fuel; and channels 2 and 4 represent the average subassemblies in the inner and outer enrichment zones respectively. Both the hot and cold pool are modeled as ‘PBLiquidVolume,’ and are connected to the Cover Gas component. The primary side of the intermediate heat exchanger is connected to the hot pool as its inlet and the cold pool as its outlet.

On the intermediate loop side, the cold leg pump, ‘Pump\_1’ in Figure 2.7, draws cold sodium from the cold storage tank to the secondary side inlet of the IHX, and the hot sodium flows into the storage tank in the hot leg. The hot leg pump, ‘Pump\_4’ in Figure 2.7, pumps hot sodium into the steam generator to produce superheated steam. As shown in Figure 2.7, the steam generator model will be highly simplified, and the power conversion cycle system will not be included in the model. As discussed earlier, to minimize the thermal disturbance from the intermediate loop to the reactor system, it is proposed to maintain the cold leg pump at a relatively constant mass flow rate, and the cold leg tank to maintain a relatively constant sodium temperature. The mass flow rate delivered by the hot leg pump will be controlled and adjusted to match electricity demand, as will be discussed later in this section.

In SAM input model, the TES tank is modeled using the SAM built-in ‘LiquidTank’ component as illustrated in Figure 2.8. As its name suggests, the LiquidTank component models a volume of

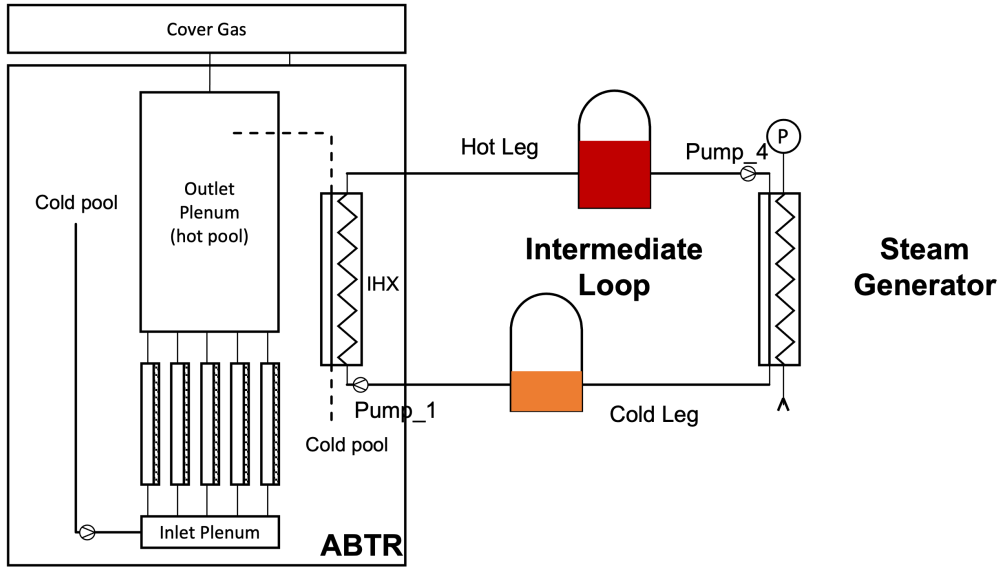


Figure 2.7: Schematic drawing of SFR/TES SAM input model.

liquid with a free surface, and tank walls as heat structures [24]. The free surface level is determined by the mass balance between inlet and outlet pipes. The various heat transfer mechanism between the fluid volume, tank walls, and ambient environment can all be adequately modeled, including the convective heat transfer between the fluid volume and the inner surface of tank walls, heat conduction across tank walls, and heat loss from tank wall outer surface to the ambient via convection and thermal radiation. For the natural circulation convective heat transfer between the liquid volume and the tank wall inner surface, several correlations exist, such as [25]. These correlations, which also requires iterative or fully coupled calculation, are currently not available for the LiquidTank component. As a very rough estimation, a Nusselt number of 20 is used. The uncertainty of this value should be further evaluated in future studies. For the outer surface, a constant ambient temperature of 300 K is assumed, and the convective heat transfer coefficient is set as a constant value of 25 W/m<sup>2</sup>-K. Again, when more information is available on the siting of the SFR/TES system, realistic data should be used for these values. The tank wall is modeled as a two-layer heat structure, with a stainless steel inner layer and a mineral wool outer layer. The thicknesses of the two layers are given in Table 2.2. The material properties of the two materials are taken from reference [21], and are summarized in Table 2.3. A separate simulation that studied the heat loss from this storage tank showed that the relative heat loss is less than 0.1 % of the reactor power, and therefore, not likely to be a concern affecting the overall efficiency of the integrated system. A similar conclusion was drawn in reference [21]. However, as noted earlier, more detailed simulations will be needed to study the tank behavior when more design information is available.

As shown in Figure 2.7, the power conversion system side is highly simplified. Only the secondary side of the steam generator is included, and the rest of the system are provided as boundary conditions. Although steam generator in the SAM input uses a highly simplified model, in order to make appropriate simplifications, it is still crucial to understand how the steam Rankine cycle performs under load following conditions. Figure 2.9 shows Westinghouse four-loop design

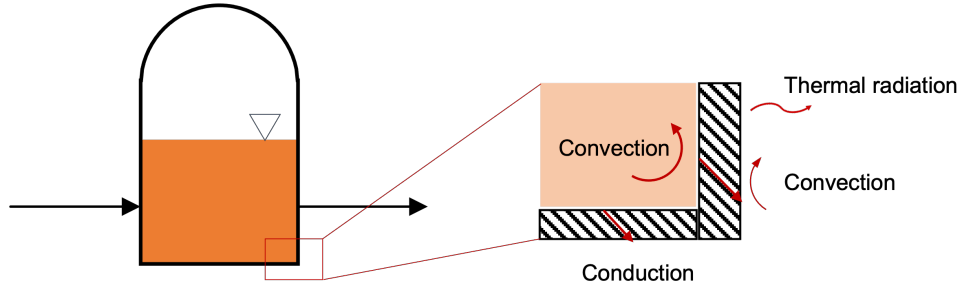


Figure 2.8: TES tank model using SAM.

Table 2.3: TES tank wall material properties

Tank Wall - Stainless Steel	
Density	7800 kg/m <sup>3</sup>
Heat Capacity	490 J/kg-K
Thermal Conductivity	21 W/m-K
Wall Insulation - Mineral Wool	
Density	160 kg/m <sup>3</sup>
Heat Capacity	840 J/kg-K
Thermal Conductivity	$0.037 + 2 \times 10^{-4}(T - 273.15)$ W/m-K; T in K.

reactor response during a 100%-50% ramp load decreasing transient with a 5% per minuate rate [26]. During the transient, generator load, as shown in Figure 2.9a, decreases as the control valves close in response to the 5%/min load decrease. Nuclear power, as shown in Figure 2.9b, decreases in response to the negative reactivity added by rod insertion because of power mismatch. On the power conversion side, steam flow decreases as the control valves close to decrease load, and feed water flow decreases to match steam and feed flows. Figure 2.9b indicates that, during the entire transient, from 100% to 50% power, the system response is quite linear, i.e., between generator load, nuclear power, and steam flow. This is not a complete surprise, because the Westinghouse design cycle efficiency does not suffer much reduction when power is reduced [27], as shown in Figure 2.10. However, it is noted that the reference steam generator of the ABTR design is different than the U-tube steam generator used in Westinghouse PWR designs. Therefore, future studies on steam generator and power conversion cycle performance during load following conditions will be needed when additional Oklo design information are available.

Based on the known experience on PWR steam Rankine cycle performance during load following as discussed above, the following model simplification and control strategy for the integrated SFR/TES system are proposed. For the steam generator, the most important behavior to model is its heat rejection rate from the primary to secondary side, while the secondary side flow is of no particular interest. Currently, we do not intend to model two-phase flow with SAM, and the secondary side water/steam flow will be simplified as single-phase flow using sodium as the surrogate



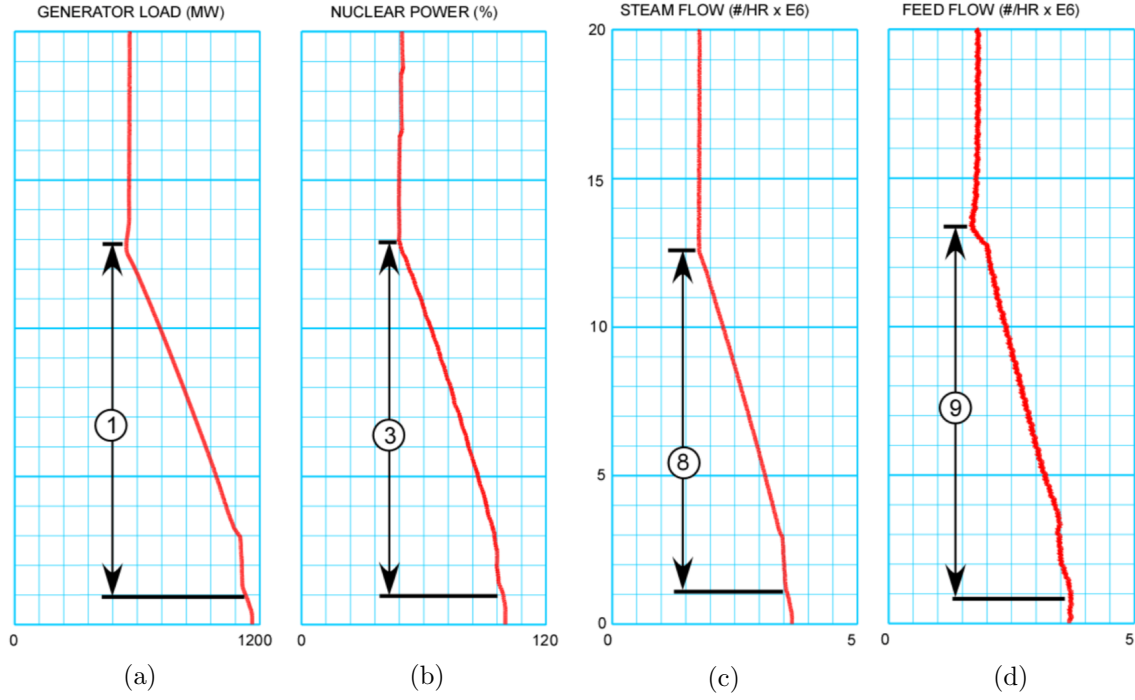


Figure 2.9: Westinghouse four-loop design response during a 100%-50% ramp load decrease transient [26]: (a) load; (b) reactor power; (c) steam flow; (d) feedwater flow. Note that the y-axis is time; while the x-axis is percentage or absolute values.

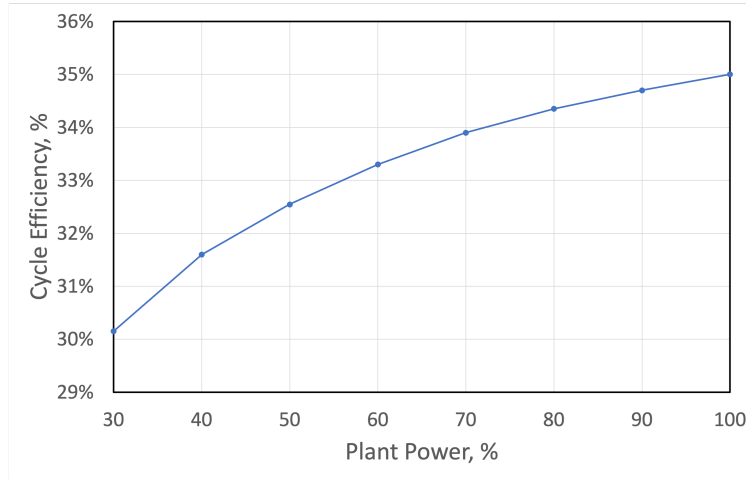


Figure 2.10: Typical 1200 MWe Pressurized Water Reactor Plant Cycle Efficiency (%) vs. Power Level (%), duplicated from [27].

fluid. To maintain a desired steam generator primary side sodium outlet temperature, the secondary side flow is given a very large flow rate with the inlet temperature to be the desired primary side sodium outlet temperature.

The control strategy to adjust the hot leg pump head is illustrated in Figure 2.11. The purpose of the control is, by adjusting hot leg pump head and therefore its mass flow rate, to match steam generator heat rejection rate with the desired rate computed from electricity demand and cycle efficiency. As illustrated in Figure 2.11, the steam generator heat rejection rate is a simulation-computed value and is monitored and sent to the control system as one of the input value. The electricity demand along with the cycle efficiency curve are combined to compute the desired steam generator heat load, also sent to the control system as an input value. The control system compares the two inputs and use a PID controller to adjust the hot leg pump head.

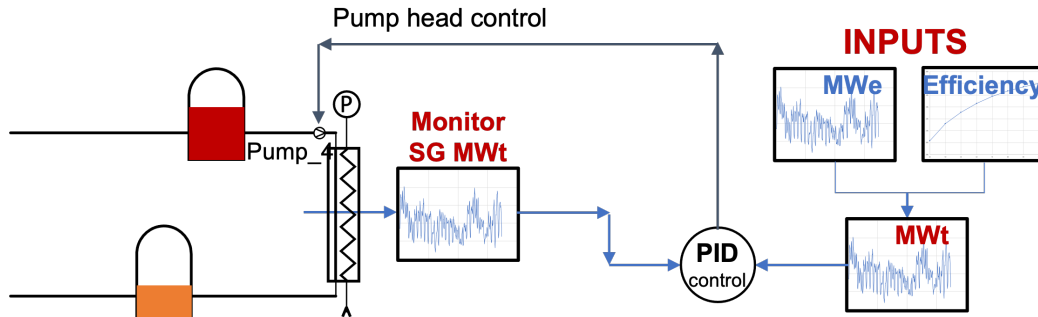


Figure 2.11: Hot leg pump heat control strategy based on monitored steam generator heat rejection rate and electricity demand.

## 2.6 Simulation Results on a ‘Typical Day’

This subsection presents a ‘typical day’ load following simulation using the established SAM input model as described in the previous subsection. For this simulation, time-varying electricity demand is taken from scaled PJM data on April 5th of 2021 (Figure 2.5), and provided as an input condition for the simulation. A predetermined cycle efficiency curve, which assumes the same shape of Figure 2.10 while the peak efficiency of 37.8 %, is also provided as input condition. The two curves are automatically combined to produce the projected thermal power requirement for the load following simulation. Because SAM uses fully implicit time integration scheme, large time step size 100 second can be used. The one-day load following simulation takes around 10-20 minutes to finish on a desktop computer. As shown in Figure 2.12, with the PID controller, SAM-predicted steam generator heat load can match the demand very well, demonstrating that the proposed integrated SFR/TES system capable of load following for the target market.

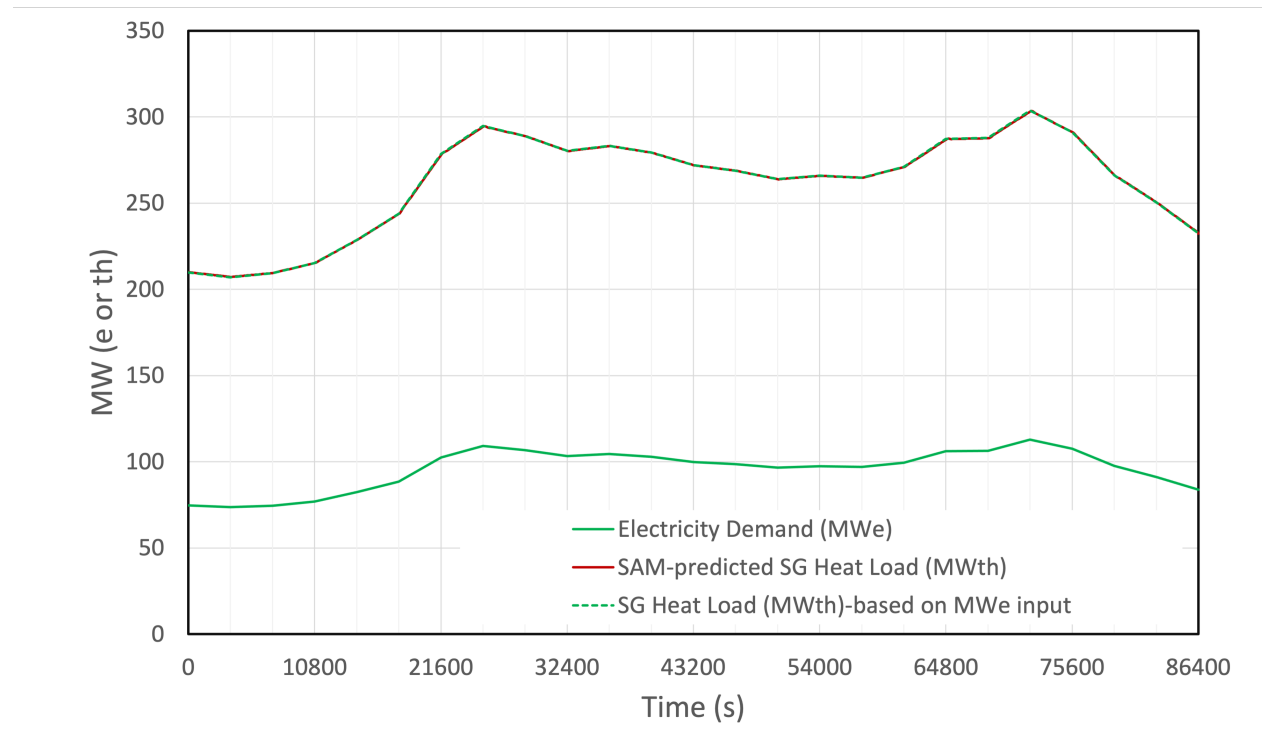


Figure 2.12: SAM simulation results on a ‘typical day,’ using proposed April 5 load following data shown in Figure 2.5.

## 2.7 Conclusions and Future Work

In this work, a preliminary modeling and simulation effort using SAM is presented to study an integrated SFR/TES system under load following conditions. The proposed integrated system consists of the reference ABTR, which operates under relatively constant condition, and two large sodium storage tanks for heat storage purpose. Existing knowledge in the solar power industry was

leveraged to design the storage tank, e.g., sizing, material, insulation, etc. A reference cylindrical tank design with a diameter of 36 m and a height of 14 m is proposed, which satisfies thermal storage needs based on the estimation using realistic PJM electricity market data. In the SAM input model, all essential subsystems relevant to the simulation of the integrated system under load following conditions are modeled, including the ABTR, TES tanks, steam generator, connecting piping and pumps. A control strategy was implemented and modeled. A PID controller controls the hot leg pump head to match steam generator heat load with the projected load computed from electricity demand and cycle efficiency. The model was used to model the transient response of the integrated system under load following conditions using the PJM April 5th, 2021 data. The simulation results showed that the system was able to perform the proposed load following.

Nevertheless, it is noted that this is still a preliminary study. Although all essential subsystems have been included, however, the modeling of some of the subsystems will be further improved as additional design information and code capabilities become available. As suggested in this study, daily or weekly reactor power ramp maneuver will most likely be needed to assist load following. To simulate reactor core power ramp, the SAM model will include the point kinetics model for reactor core behavior and include the external reactivity from control rod movement. Because of the varying reactor power output, the thermal response of the primary and consequently the intermediate loop and power conversion system will all be affected. This requires the development of a control strategy to maintain a stable operating condition of the integrated system. In addition, as more design information are available on the power conversion system, more detailed studies will be needed to understand better the steam Rankine cycle behavior during load following conditions, e.g., its thermal response, efficiency, control, etc. Another important aspect not included in this preliminary study is the economics of the integrated system, which is needed to address the extra cost of TES system, the trade-off between different TES tank sizes, etc.

## **3 Westinghouse Project: Direct resolution of surface roughness**

### **3.1 Introduction**

Surface roughness plays a critical role in many engineering processes. From a nuclear engineering perspective, one such example can be found in the manufacturing of the coated cladding for the Accident-Tolerant Fuel (ATF). A better understanding on the roughness effects will directly benefit the performance optimization of the related fuel product while reducing the production costs. Currently effects of surface roughness on flow and convective heat transfer are modeled based on the developed correlations and wall functions which are all dependent (and limited) on the range of flow and relative surface roughness conditions applied in experiments. The conditions for real applications can be out of the experimentally obtained ranges, or not comparable because of the additional (not tested) surface features. This introduces uncertainties in modeling. Though computationally demanding, Direct Numerical Simulations (DNS) is currently the most accurate approach to simulate the related turbulent flow physics, which directly solves the Navier-Stokes equations and involves no assumptions/closures about the turbulence modeling. Thanks to the rapid development of high-performance computing (HPC), the DNS capability has now caught up to address the thermal-fluid

problems of direct engineering relevance. Leveraging the DNS capability offered by the NEAMS signature CFD code, Nek5000 [28, 29], the goal of this investigation is to establish and develop best practices for direct modeling of rough surface effects on the flow configurations (including velocity profiles) and evaluation of flow resistances at a reasonable Reynolds numbers. These practices will enable further direct modeling of more complex domains and interactive phenomena such as conjugate heat transfer in fuel rod assemblies with rough cladding surfaces in the near future.

### 3.2 Flow solver: Nek5000

Nek5000 is used in this work to perform the DNS for the pipe flow with both smooth and rough inner wall. Nek5000 is an open source CFD code based on the spectral element method (SEM) [30] with a long history of use in reactor thermal-hydraulics research [31]. SEM combines the accuracy of spectral methods with the domain flexibility of the finite element method. In Nek5000 calculations, the domain is discretized into  $E$  curvilinear hexahedral elements, in which the solution is represented as a tensor product of  $N^{th}$ -order Lagrange polynomials based on the Gauss-Lobatto-Legendre (GLL) nodal points, leading to a total number of grid points  $n = EN^3$ . Nek5000 was designed from the outset to take advantage of distributed-memory platforms. It is highly parallel and has been previously applied to a wide range of problems to gain unprecedented insight into the physics of turbulence in complex flows [31]. The time-stepping scheme of Nek5000 is semi-implicit: the diffusion terms of the Navier-Stokes equations are treated implicitly by using a  $k^{th}$ -order backward difference formula (*BDFk*), while nonlinear terms are approximated by a  $k^{th}$ -order extrapolation (*EXTk*) [32]. Nek5000 is highly scalable on leadership class supercomputers, which makes it an ideal candidate to carry out the intended DNS calculations on wall roughness effect at potentially high Reynolds numbers.

We consider the pressure-driven incompressible flow of a viscous Newtonian fluid in circular pipes where the governing equations are the time-dependent Navier-Stokes equations given by

$$\frac{\partial u_i}{\partial x_i} = 0 \quad (4)$$

$$\frac{\partial u_i}{\partial t} + \frac{\partial}{\partial x_j}(u_i u_j) = -\frac{1}{\rho} \frac{\partial p}{\partial x_i} + \frac{\partial}{\partial x_j} \left[ \nu \left( \frac{\partial u_i}{\partial x_j} + \frac{\partial u_j}{\partial x_i} \right) \right] \quad (5)$$

Continuous validation and verification studies have been conducted over years for Nek5000 for various geometries of interest to nuclear engineers, such as the rod bundles with spacer grid and mixing vanes. For example, the 2012 KAERI Matis experiment has tested the CFD predictions of the mixing flow in a complex geometry of subchannel behind a swirl-vane spacer grid. The Nek5000 LES submissions scored highly in the blind benchmarks [33]. More recently, Busco et al. performed the validation of the wall resolved LES for the flow through a 5x5 fuel rod bundle with SGMV at a Reynolds number of 14,000 [34]. Excellent agreement was obtained between Nek5000 results and the particle image velocimetry (PIV) data. Meanwhile, Kraus et al. reported a comprehensive DNS study for the 5x5 bare rod bundle with the Nek5000 at a Reynolds number of 19,000 [29]. Built

upon the great track record of Nek5000 in predicting flow physics in realistic reactor geometries, this study attempts to expand Nek5000 applicability to study the wall roughness effect for reactor relevant geometries.

### 3.3 Problem Description

The cold spray production process applies a 10 to 30-micron layer of Cr on the current Zr based alloy fuel cladding. This Cr layer provides a significant corrosion benefit during normal operation and makes the cladding more tolerant to beyond design basis accident conditions which lead to the total destruction of current Zr only cladding. After the Cr is applied, the surface has about 4-micron roughness which is then polished to the current cladding specification of 0.2 microns. This represents a large cost in polishing materials, machinery and production time considering that 10 million feet per year is required. Since the laminar boundary sub-layer is expected to be in the range of 1 to 2 microns, polishing to 0.2-microns is likely to be an unnecessary expense. Performing testing at prototypical PWR conditions for this level of roughness is very difficult, time consuming and expensive. The application of Computational Fluid Dynamics (CFD) modelling to this problem is a significantly faster, much more cost-effective and more comprehensive approach to answering this question. Similar investigations have been performed previously using DNS for flat channel flows with positive results [35, 36]. This strongly indicates that the proposed extension of applying the technique to reactor-relevant geometries will be successful. As a first step, this study will consider the DNS investigations of a pipe geometry with both the smooth and the rough inner walls.

To properly resolve all the relevant turbulence fluctuations, the pipe needs to be sufficiently long. The smooth pipe has been numerically investigated with the DNS by several authors. The first example can be found in Eggels et al. [37] where a smooth pipe of a  $10R$  length is simulated at a Reynolds number 5,300 based on the mean axial velocity and pipe diameter. In contrast to the fully developed channel flow, It was found out that the mean axial velocity profile does not follow the log-law at this specific Reynolds number, which is also confirmed by more recent studies [28]. Since the experimental study has revealed the existence of large fluid motions ranging from  $5R$  to  $20R$  [38], the pipe length is selected to be  $25R$  herein following the work of El Khoury et al. [28]. To demonstrate the related numerical capabilities, especially the meshing technique in representing the wall roughness elements, a relatively low Reynolds of 5,300 is chosen for the purpose of quick testing. It is noted that the corresponding friction Reynolds number,  $Re_\tau = 180$ , matching the flow condition investigated in the pioneering DNS study of Kim et al. [39].

The domain discretization leads to a total number of 53,328 spectral elements, which involves 46% more mesh cells as in the work of El Khoury et al. [28]. This is because that we need to apply the mesh morphing treatment on the smooth pipe mesh to introduce the wall roughness elements. Thus the total mesh count will be the same in both our smooth and rough pipe cases. Relatively high mesh cell count will help better resolve the eddies induced by the wall roughness structures. The cross-sectional view of the computational grid is shown in Figure 3.1.



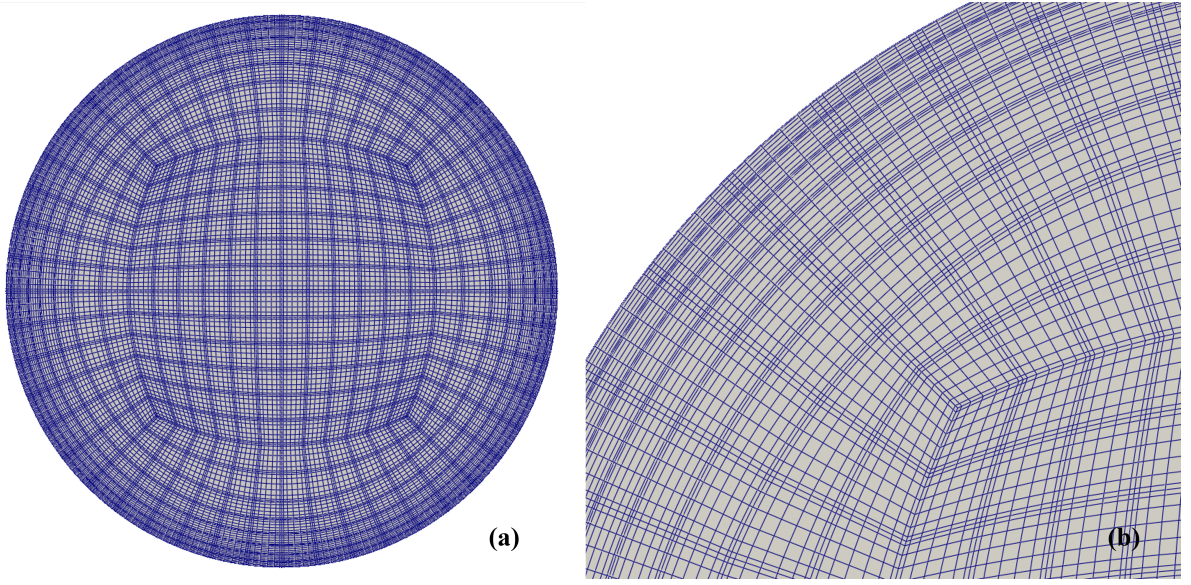


Figure 3.1: Cross-sectional view of the computational mesh at a polynomial order,  $N = 7$ : (a) overview, (b) zoom-in view.

The rough pipe case is established by deforming the near wall mesh from the smooth pipe case. The relative roughness is defined as  $K = \epsilon/D$ , where  $\epsilon$  is the characteristic roughness height and  $D$  is the pipe diameter. The specific relative roughness value is 0.04. A hemispheric shape is assumed for the roughness elements. The whole procedure of mesh morphing is summarized as follows:

- Determine the centers of wall roughness elements based on the intended relative roughness;
- For each grid point inside the domain, a projected wall point is determined with respect to the pipe centerline;
- Find out the required displacement for the projected wall point based on the locations of the wall point, the nearest roughness center, and the pipe centerline
- Decide the displacement of the grid point of interest based on its distance from the projected wall point;
- Smooth the transition from the roughness elements to the wall surface not deformed;

To ensure the above mesh morphing scheme works, special care has to be taken for the near region where the related grid points should be aligned along the wall normal direction. Figure 3.2 shows the pattern of roughness element distribution on the pipe surface. The average distance between two nearby roughness elements is about  $5\epsilon$  along the circumferential and axial direction. Figure 3.3 illustrates how the interior mesh looks like after the mesh morphing treatment. A smoothed step function (Eq. 6) is used to diffuse the mesh morphing in the wall normal direction, and the related transition can be seen in Figure 3.4 which provides a detailed view around the wall roughness elements.

$$f = 1 - \tanh^2\left(\frac{w_d}{\epsilon}\right) \quad (6)$$

where  $w_d$  is the wall distance.

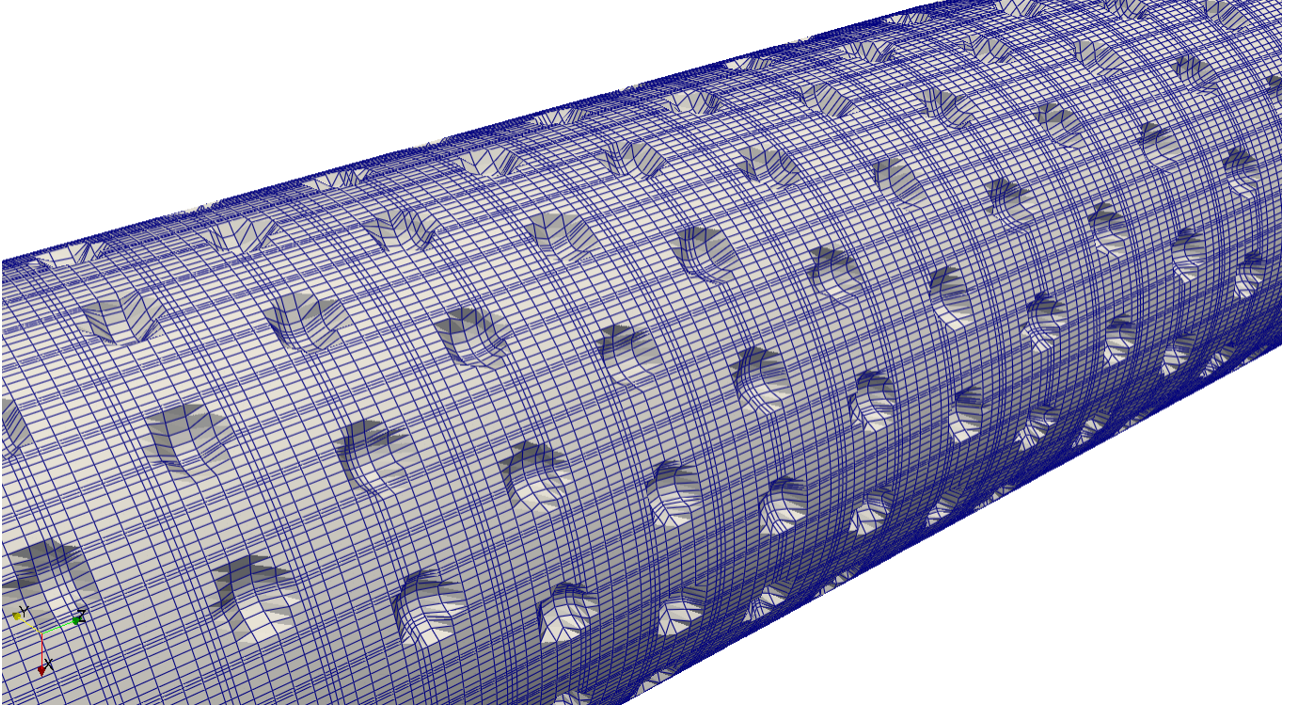


Figure 3.2: The rough pipe mesh with staggered roughness elements on the wall surface.

### 3.4 Results

The DNS is first carried out for the smooth pipe. To introduce the needed velocity fluctuations, the simulation case started at a higher Reynolds number, and the Reynolds number was then reduced to the intended value of 5,300. The smooth pipe case is simulated for about 240 convective time units. One convective time unit is defined as the physical time the mean flow takes to move the distance of one hydraulic diameter. Figure 3.5 shows the instantaneous velocity field from the smooth pipe DNS. Large scale fluid motions dominate the central region while finer scales exist close to the pipe wall. Once the simulations reached the steady state, mean axial velocity was extracted and plotted against the Law of the Wall (LotW) profile shown in Figure 3.6. The log-law profile here is



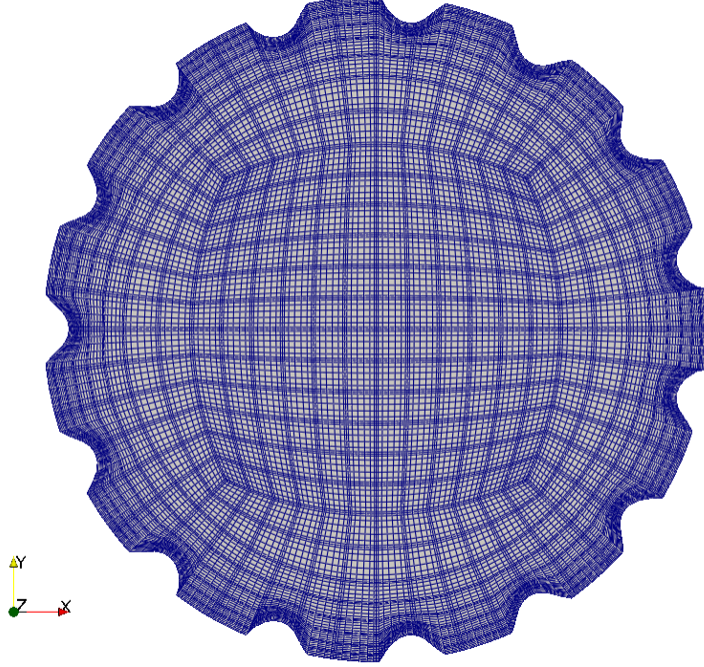


Figure 3.3: Cross-sectional view of the computational mesh from the mesh morphing.

described by Eq. 7 assuming a  $\kappa$  of 0.41 and  $C$  of 5.2 that are typical for turbulent channel flow. It is noticed that the mean axial velocity agrees well with the LotW in the viscous sublayer while deviates significantly in the log-law region. The same observation was also reported in previous pipe DNS research [37, 28], which is an outcome of the relatively low Reynolds number. As the Reynolds number increases, the mean axial velocity is expected to converge to the LotW profile as in the channel flow [28].

$$u^+ = \frac{1}{\kappa} \ln(y^+) + C \quad (7)$$

One of the primary objectives in the wall roughness study is to understand the corresponding impact on the pressure loss, or the Darcy friction factor in a dimensionless sense. The postprocessing of DNS dataset reveals a friction factor,  $f_D = 0.0372$ , in the smooth pipe at the Reynolds number of 5,300. As a reference, the Moody diagram predicts a friction factor of 0.0367 at the same Reynolds number, with only a 1.4% difference. The Moody diagram is considered accurate for the friction factors in smooth pipes, and the excellent agreement between its prediction and the Nek5000 DNS results helps place a sound foundation as we move on to the rough pipe simulations.

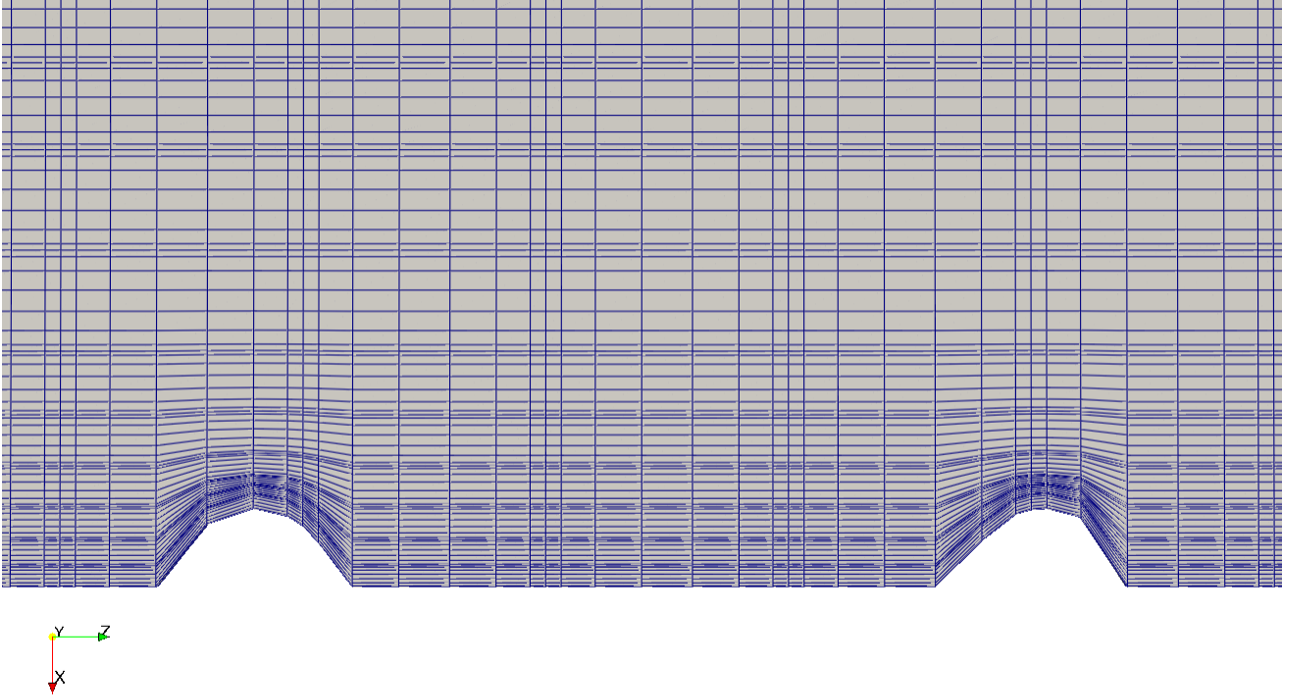


Figure 3.4: Detailed view on the mesh around the wall roughness elements.

The rough pipe mesh is created using the aforementioned mesh morphing scheme, and the resulting mesh can be found in Figures 3.2 to 3.4. The overall mesh cell count is the same in both the smooth and rough pipe case. Due to the mesh deformation introduced, the time step size used in rough pipe simulations is relatively smaller due to the stability considerations. A staggered pattern is considered for the roughness elements so that there is a longer distance after the roughness element to allow for the flow re-attachment. A comparison of the velocity field from the smooth and rough pipes is presented in Figure 3.7. As expected, the introduction of wall roughness elements generates considerable amount of finer scales, especially in the near wall region. The overall turbulence field is also more agitated in the rough pipe as compared to that in the smooth pipe. The flow separation is observed in the wakes of roughness elements. A detailed view of the flow field around the roughness elements is illustrated in Figure 3.8 where the vectors indicate the local velocity directions. A friction factor,  $f_D = 0.0977$ , is obtained from the rough pipe DNS. The reference value from the Moody diagram is 0.0693 considering a relative roughness of 0.04. This large difference suggests the need of further investigations in this matter as there are many factors that can impact the overall pressure loss, such as the roughness shape, packing density, aspect ratio, to name a few. For example, a comparison case modeling the surface roughness elements as cavities is also simulated (shown in Figure 3.9). It is observed that the corresponding turbulence field resembles that in the smooth pipe, and the friction factor,  $f_D = 0.0445$ , is much lower than the case where roughness elements are modeled as bumps. All the friction factor results are summarized in Table 3.1.

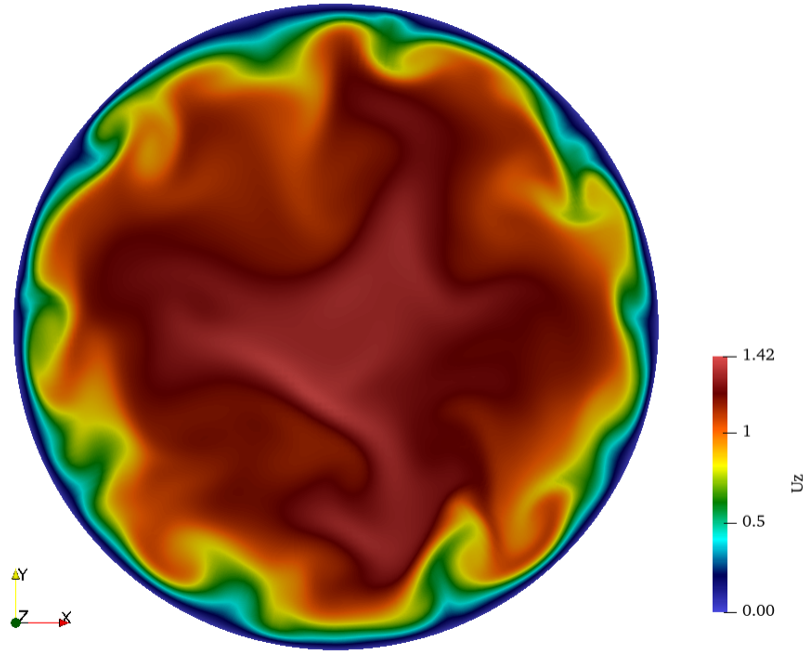


Figure 3.5: A snapshot of the instantaneous velocity field from the smooth pipe DNS.

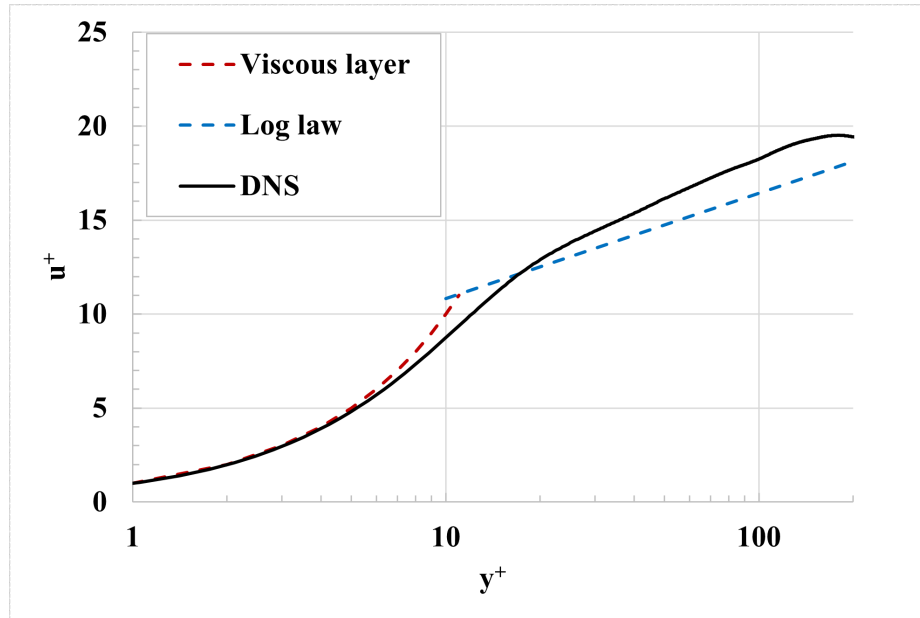


Figure 3.6: Mean axial velocity in the near wall region from the smooth pipe DNS.

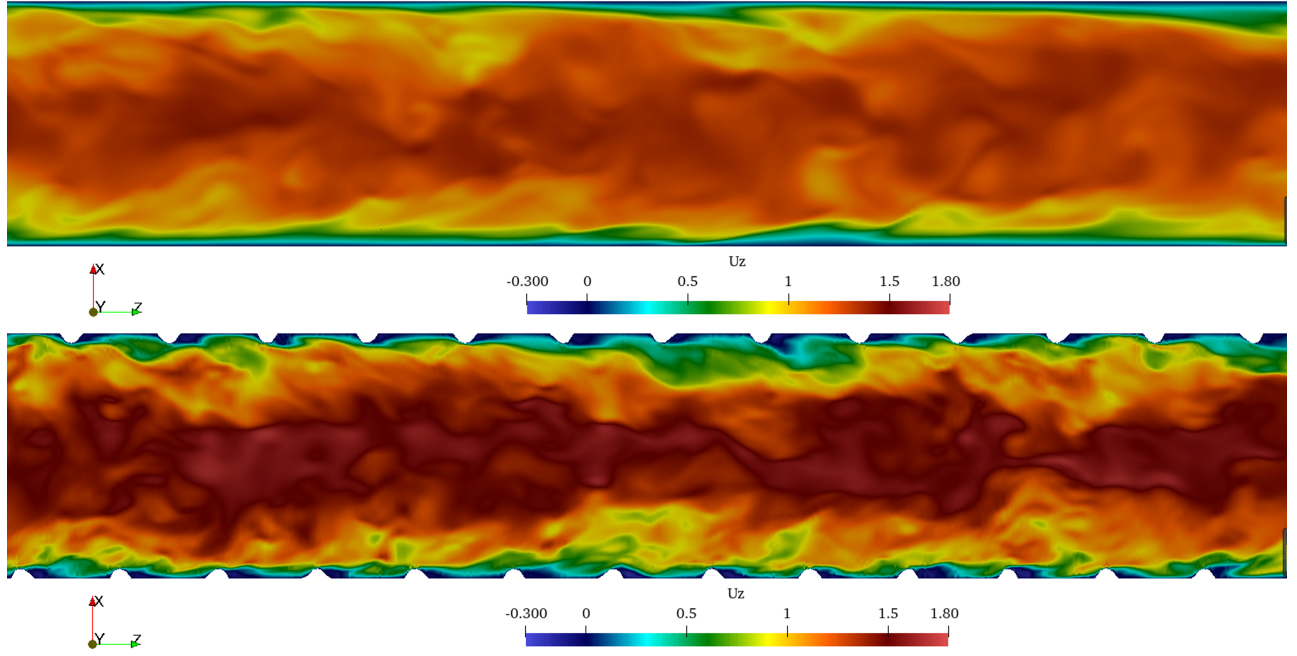


Figure 3.7: Comparison of the velocity field from the smooth and rough pipes in the axial direction.

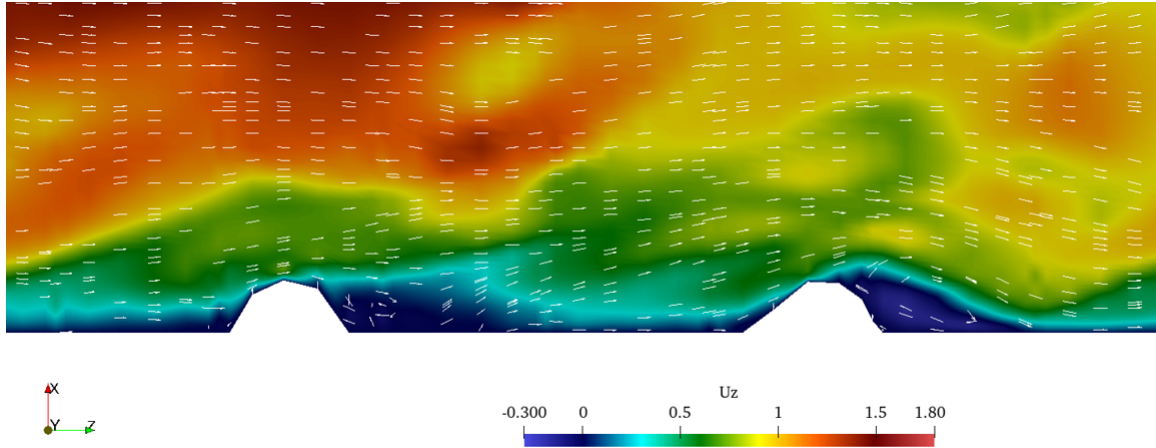


Figure 3.8: Circulations observed around the wall roughness elements.

### 3.5 Conclusions

To facilitate closer collaborations with nuclear industry partners, this study explores the Nek5000 capability in simulating the wall roughness effect, that will ultimately aid the polishing process of Accident-Tolerant Fuel (ATF). The readiness of Nek5000 has been successfully demonstrated in this Center of Excellence effort. It is feasible to produce the needed computational mesh of a rough pipe with prescribed roughness elements through the mesh morphing treatment. A series of distributed hemispheric roughness elements is considered in the current work. The same meshing

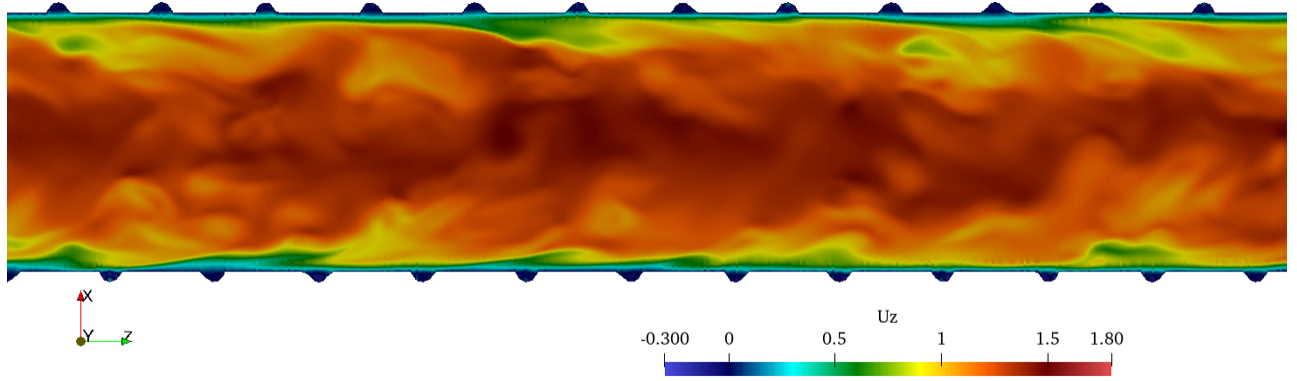


Figure 3.9: A rough pipe modeling surface roughness elements as cavities.

Table 3.1: Darcy friction factors in pipe geometry ( $Re = 5,300$ ,  $\epsilon = 0.04$ )

Pipe Surface	$f_D$
Smooth	0.0372
Roughness elements as bumps	0.0977
Roughness elements as cavities	0.0445

scheme can be also applicable for cases with random roughness distribution. The turbulence field is examined for both the smooth and rough pipes. The friction factors can be extracted from the corresponding DNS. An excellent agreement of the friction factor is noticed for the smooth pipe between the DNS results and Moody diagram while large deviation still exists for the rough pipe case. Future investigations will explore the effects of roughness element shape, packing density, etc. Moreover, the wall roughness study will be also extended to the reactor relevant geometries, such as the fuel rod bundle in the near future.

## Acknowledgments

The authors would like to thank David Hawn and Patrick Everett from Oklo for providing the conceptual design of the integrated SFR/TES system, and for their fruitful discussions throughout the work. The authors would also like to thank Milorad Dzodzo from Westinghouse for support and guidance on the simulations of wall resolved roughness.

Argonne National Laboratory's work was supported by the U.S. Department of Energy, Office of Nuclear Energy, Nuclear Energy Advanced Modeling and Simulation (NEAMS) program through the Center of Excellence for Thermal-fluids Applications in Nuclear Energy, under contract DE-AC02-06CH11357.



# References

- [1] J. Fang, L. Brockmeyer, G. Hu, L. Zou, R. Hu, and E. Merzari, “Center of excellence collaboration projects: Second wave,” Tech. Rep. ANL/NSE-20/22, Argonne National Laboratory, Lemont, IL, June 2020.
- [2] D. Shaver, R. Hu, P. Vegendla, L. Zou, and E. Merzari, “Initial industry collaborations of the center of excellence,” Tech. Rep. ANL/NSE-19/15, Argonne National Laboratory, Lemont, IL, June 2019.
- [3] A. Lokhov, “Technical and economic aspects of load following with nuclear power plants,” tech. rep., Nuclear Energy Agency, June 2011.
- [4] A. Lokhov, “Load-following with nuclear power plants,” *NEA News*, vol. 29, pp. 18–20, 2011.
- [5] World Nuclear Association, “Nuclear Power in France.” <https://world-nuclear.org/information-library/country-profiles/countries-a-f/france.aspx>, January 2021.
- [6] International Atomic Energy Agency, “Non-baseload operation in nuclear power plants: Load following and frequency control modes of flexible operation,” Tech. Rep. No. NP-T-3.23, 2018.
- [7] P. Denholm, J. C. King, C. F. Kutcher, and P. P. Wilson, “Decarbonizing the electric sector: Combining renewable and nuclear energy using thermal storage,” *Energy Policy*, vol. 44, pp. 301–311, 2012.
- [8] C. Forsberg, P. Sabharwall, and A. Sowder, “Separating nuclear reactors from the power block with heat storage: A new power plant design paradigm,” Tech. Rep. MIT-ANP-TR-189, Center for Advanced Nuclear Energy System, Massachusetts Institute of Technology, 2020.
- [9] C. Forsberg and P. Sabharwall, “Heat storage options for sodium, salt and helium cooled reactors to enable variable electricity to the grid and heat to industry with base-load reactor operations,” Tech. Rep. MIT-ANP-TR-181, Center for Advanced Nuclear Energy System, Massachusetts Institute of Technology, 2018.
- [10] J. Edwards, H. Bindra, and P. Sabharwall, “Exergy analysis of thermal energy storage options with nuclear power plants,” *Annals of Nuclear Energy*, vol. 96, pp. 104–111, 2016.
- [11] S. A. Alameri, J. C. King, A. K. Alkaabi, and Y. Addad, “Prismatic-core advanced high temperature reactor and thermal energy storage coupled system—a preliminary design,” *Nuclear Engineering and Technology*, vol. 52, no. 2, pp. 248–257, 2020.

- [12] G. Alva, Y. Lin, and G. Fang, “An overview of thermal energy storage systems,” *Energy*, vol. 144, pp. 341–378, 2018.
- [13] <https://natriumpower.com>, 2021.
- [14] R. Hu, L. Zou, G. Hu, D. Nunez, T. Mui, and T. Fei, “SAM theory manual,” Tech. Rep. ANL/NSE-17/4 Rev. 1, Argonne National Laboratory, Lemont, IL, February 2021.
- [15] Y. Chang, P. Finck, and Grandy, “Advanced burner test reactor preconceptual design report,” Tech. Rep. ANL-ABR-1, ANL-AFCI-173, Argonne National Laboratory, 2006.
- [16] K. Niedermeier, J. Flesch, L. Marocco, and T. Wetzel, “Assessment of thermal energy storage options in a sodium-based CSP plant,” *Applied thermal engineering*, vol. 107, pp. 386–397, 2016.
- [17] <https://www.pjm.com/about-pjm/who-we-are>, 2021.
- [18] Z. Fan, T. Horger, J. Bastian, and A. Ott, “An overview of pjm energy market design and development,” in *2008 Third International Conference on Electric Utility Deregulation and Restructuring and Power Technologies*, pp. 12–17, IEEE, 2008.
- [19] O. Foust, ed., *Sodium-NaK engineering handbook. Volume III. Sodium systems, safety, handling, and instrumentation*. Gordon & Breach Science Pub, 1978.
- [20] J. Schulte-Fischedick, R. Tamme, and U. Herrmann, “CFD analysis of the cool down behaviour of molten salt thermal storage systems,” in *Energy Sustainability*, vol. 43208, pp. 515–524, 2008.
- [21] F. Zaversky, J. García-Barberena, M. Sánchez, and D. Astrain, “Transient molten salt two-tank thermal storage modeling for CSP performance simulations,” *Solar Energy*, vol. 93, pp. 294–311, 2013.
- [22] Solar Millennium, “The parabolic trough power plants andasol 1 to 3: The largest solar power plants in the world – Technology premiere in Europe.” <http://large.stanford.edu/publications/power/references/docs/Andasol1-3engl.pdf>.
- [23] G. Hu, G. Zhang, and R. Hu, “Reactivity feedback modeling in SAM,” Tech. Rep. ANL-NSE-19/1, Argonne National Laboratory, Lemont, IL, February 2019.
- [24] R. Hu, L. Zou, G. Hu, and T. Mui, “SAM user’s guide,” Tech. Rep. ANL/NSE-19/18 Rev. 1, Argonne National Laboratory, Lemont, IL, February 2021.
- [25] J. S. McDonald and T. Connolly, “Investigation of natural convection heat transfer in liquid sodium,” *Nuclear Science and Engineering*, vol. 8, no. 5, pp. 369–377, 1960.
- [26] U.S. Nuclear Regulatory Commission, “0523 - R504P - Westinghouse Advanced Technology. Chapter 5: Westinghouse Four-Loop Design Transients. Available online at: <https://www.nrc.gov/docs/ML1121/ML11216A094.pdf>,” Tech. Rep. ML11216A094, August 2011.

- [27] C. Forsberg, “Light water reactor heat storage for peak power and increased revenue: Focused workshop on near term options,” Tech. Rep. MIT-ANP-TR-170, Center for Advanced Nuclear Energy System, Massachusetts Institute of Technology, July 2017.
- [28] G. K. El Khoury, P. Schlatter, A. Noorani, P. F. Fischer, G. Brethouwer, and A. V. Johansson, “Direct Numerical Simulation of Turbulent Pipe Flow at Moderately High Reynolds Numbers,” *Flow, Turbulence and Combustion*, vol. 91, no. 3, pp. 475–495, 2013.
- [29] A. Kraus, E. Merzari, T. Norddine, O. Marin, and S. Benhamadouche, “Direct numerical simulation of fluid flow in a 5x5 square rod bundle,” *International Journal of Heat and Fluid Flow*, vol. 90, p. 108833, 2021.
- [30] A. T. Patera, “A spectral element method for fluid dynamics: Laminar flow in a channel expansion,” *Journal of Computational Physics*, vol. 54, pp. 468–488, jun 1984.
- [31] E. Merzari, A. Obabko, P. Fischer, N. Halford, J. Walker, A. Siegel, and Y. Yu, “Large-scale large eddy simulation of nuclear reactor flows: Issues and perspectives,” *Nuclear Engineering and Design*, vol. 312, pp. 86–98, feb 2017.
- [32] L. W. Ho, *A Legendre spectral element method for simulation of incompressible unsteady viscous free-surface flows*. PhD thesis, Massachusetts Institute of Technology, 1989.
- [33] A. Obabko, P. Fischer, O. Marin, E. Merzari, and D. Pointer, “Verification and Validation of Nek5000 for T-junction, Matis, SIBERIA, and Max Experiments,” in *16th International Topical Meeting on Nuclear Reactor Thermal Hydraulics (NURETH-16)*, (Chicago, IL), American Nuclear Society, 2015.
- [34] G. Busco, E. Merzari, and Y. A. Hassan, “Invariant analysis of the Reynolds stress tensor for a nuclear fuel assembly with spacer grid and split type vanes,” *International Journal of Heat and Fluid Flow*, vol. 77, pp. 144–156, jun 2019.
- [35] S. Wu, K. T. Christensen, and C. Pantano, “Modelling smooth- and transitionally rough-wall turbulent channel flow by leveraging inner–outer interactions and principal component analysis,” *Journal of Fluid Mechanics*, vol. 863, pp. 407–453, 2019.
- [36] A. V. Mishra and I. A. Bolotnov, “DNS of turbulent flow with hemispherical wall roughness,” *Journal of Turbulence*, vol. 16, no. 3, pp. 225–249, 2015.
- [37] J. G. M. Eggels, F. Unger, M. H. Weiss, J. Westerweel, R. J. Adrian, R. Friedrich, and F. T. M. Nieuwstadt, “Fully developed turbulent pipe flow: a comparison between direct numerical simulation and experiment,” *Journal of Fluid Mechanics*, vol. 268, pp. 175–210, 1994.
- [38] K. C. Kim and R. J. Adrian, “Very large-scale motion in the outer layer,” *Physics of Fluids*, vol. 11, pp. 417–422, jan 1999.
- [39] J. Kim, P. Moin, and R. Moser, “Turbulence statistics in fully developed channel flow at low Reynolds number,” *Journal of Fluid Mechanics*, vol. 177, pp. 133–166, 1987.





**Nuclear Science and Engineering Division**

Argonne National Laboratory  
9700 South Cass Avenue, Bldg. 208  
Argonne, IL 60439

[www.anl.gov](http://www.anl.gov)



Argonne National Laboratory is a U.S. Department of Energy  
laboratory managed by UChicago Argonne, LLC